

Model Evaluation of a Transformable CubeSat for Nonholonomic Attitude Reorientation Using a Drop Tower

Yuki Kubo^{1*}, Tsubasa Ando², Hirona Kawahara³, Shu Miyata²,
Naoya Uchiyama², Kazutoshi Ito⁴, Yoshiki Sugawara²

^{1*}Institute of Space and Astronautical Science, Japan Aerospace Exploration Agency,
3-1-1 Yoshinodai, Chuo-ku, Sagamihara, 252-5210, Kanagawa, Japan.

²Department of Mechanical Engineering, Aoyama Gakuin University, 5-10-1 Fuchinobe,
Chuo-ku, Sagamihara, 252-5258, Kanagawa, Japan.

³Department of Physical Sciences, Aoyama Gakuin University, 5-10-1 Fuchinobe,
Chuo-ku, Sagamihara, 252-5258, Kanagawa, Japan.

⁴Department of Applied Mechanics and Aerospace Engineering, Waseda University, 3-4-1
Okubo, Shinjuku-ku, 169-8555, Tokyo, Japan.

*Corresponding author(s). E-mail(s): kubo.yuki@jaxa.jp;

Contributing authors: c5624137@aoyama.jp; a5921039@aoyama.jp; a5622118@aoyama.jp;
c5623158@aoyama.jp; kazu-physics6.97@fuji.waseda.jp; sugawara@me.aoyama.ac.jp;

Abstract

This paper presents a design for a drop tower test to evaluate a numerical model for a structurally reconfigurable spacecraft with actuatable joints, referred to as a transformable spacecraft. A mock-up robot for a 3U-sized transformable spacecraft is designed to fit in a limited time and space of the microgravity environment available in the drop tower. The robot performs agile reorientation, referred to as nonholonomic attitude control, by actuating joints in a particular manner. To adapt to the very short duration of microgravity in the drop tower test, a successive joint actuation maneuver is optimized to maximize the amount of attitude reorientation within the time constraint. The robot records the angular velocity history of all four bodies, and the data is analyzed to evaluate the accuracy of the numerical model. We confirm that the constructed numerical model sufficiently replicates the robot's motion and show that the post-experiment model corrections further improve the accuracy of the numerical simulations. Finally, the difference between this drop tower test and the actual orbit demonstration is discussed to show the prospect.

Keywords: Drop tower test, Reconfigurable spacecraft, Attitude reorientation, Nonholonomic system, Particle swarm optimization, CubeSat

1 Introduction

Novel space exploration technologies have grown rapidly and widely in recent years. A transformable spacecraft is one such architecture, enabling a spacecraft to reconfigure itself with actuatable joints. We can expect the transformable spacecraft to perform multi-objective operations with highly redundant actuators. The Transformer research group, organized by JAXA and universities in Japan, has proposed and studied a concept of such a highly redundant "Transformer" (Sugawara et al, Oct. 2020). The other group, Tokyo Institute of Technology, launched HIBARI in 2021 (WATANABE et al, 2023; Kobayashi et al, 2024). HIBARI had only four degrees of freedom actuators, but it carried out important and insightful orbit demonstrations with actuatable mechanisms.

One key technology for the transformable spacecraft is "nonholonomic attitude control," where the spacecraft can reorient its attitude by successive joint actuation (the details are described in Section 3.1). Physical properties such as mass, position of the center of mass, and moment of inertia determine the direction and amount of the reorientation. Therefore, understanding the fidelity and accuracy of the numerical model is important for the maneuver design. In general, a spacecraft is composed of many components and is not necessarily precisely modeled

due to time and cost constraints. Moreover, some components, such as flexible harnesses and propellants, take much work to model. Thus, measuring such physical properties through ground tests and operations in orbit is essential.

This article describes a method of model evaluation using a drop tower facility. We introduce the experiment's design and analyze the obtained results. Section 2 describes the facility of the drop tower, the design of a transformable robot, and a release mechanism. Section 3 first introduces an overview of the nonholonomic attitude control and is followed by physical modeling and maneuver designs using the particle swarm optimization. Section 4 explains setups of the experiment and is followed by results and discussions in Section 5 and 6.

2 Design of hardware

This section describes the experiment facility and the hardware design.

2.1 Facility of the drop tower

A drop tower is less costly than an orbit demonstration and a parabolic flight by an airplane. In addition, the test hardware can be refurbished on the ground during relatively long intervals of capsule drops. For these reasons, we adopted the drop tower as a test facility for this experiment. In particular, the drop tower facility COSMOTORRE in

Hokkaido, Japan, was chosen for this experiment. The tower and the drop capsule are shown in Fig. 1, and their specification is overviewed in Table 1. Instruments for the experiment are equipped in the inner capsule. The inner capsule is installed inside the outer capsule, which reduces air drag during free fall.

Table 1 Specification overview of COSMOTORRE

Drop height	45 m
Micro-G duration	2.5 sec
Micro-G quality	$> 10^{-3}$ G
Payload size	$\phi 50 \times 105$ cm
Maximum payload mass	400 kg

2.2 Design of the transformable robot

The transformable robot in this experiment is designed to satisfy some requirements imposed by the drop tower facility:

- To finish a set of maneuvers during the micro-G duration of the drop tower (about 2.5 sec)
- To fit in the inner capsule envelope ($\phi 50 \times 105$ cm) during the entire maneuvers

The overview and dimensions of the designed robot are shown in Fig. 2 and 3. The robot is composed of four bodies with three actuatable joint units. Each joint unit comprises a servomotor, two absolute angle sensors (at both ends of the rotational axis of the motor), and bracket structures. The total mass is 2,847 g. The frame structure is

composed of universal aluminum frames that can endure the landing impact at the end of the drop test. The robot’s size is compatible with 3U Cube-Sat, whereas the length in x -direction is elongated due to the release mechanism.

The joint is actuatable in a range of 90 degrees, with 20 kgf·cm torque. With this setup, the average angular velocity of the joint is 150-200 deg/s; thus, the possible total angular displacement during 2.5 sec is 375-500 deg.

MEMS gyroscope boards equipped with InvenSense MPU-6050 are mounted on all four bodies. Parameter specifications of the MPU-6050 are shown in Table 2.

Table 2 Specifications of InvenSense MPU-6050

Parameters	Values
Full-scale range	± 500 deg/s
Full-scale bit length	16 bits
Bandwidth of low pass filter	5 Hz
Maximum sampling rate	1 kHz
Sensitivity scale factor tolerance	$\pm 3\%$
Linear acceleration sensitivity	0.1 deg/s/g

Two lasers are mounted orthogonally on body 2. The laser ray is projected on graph paper attached to the side walls of the test space and captured by cameras, which allows us to estimate the release velocity of the robot.

The robot has two microprocessors. Arduino micro mounted on the sequence control board controls the entire maneuver sequence of the robot. On the other hand, Teensy 4.1, mounted on the

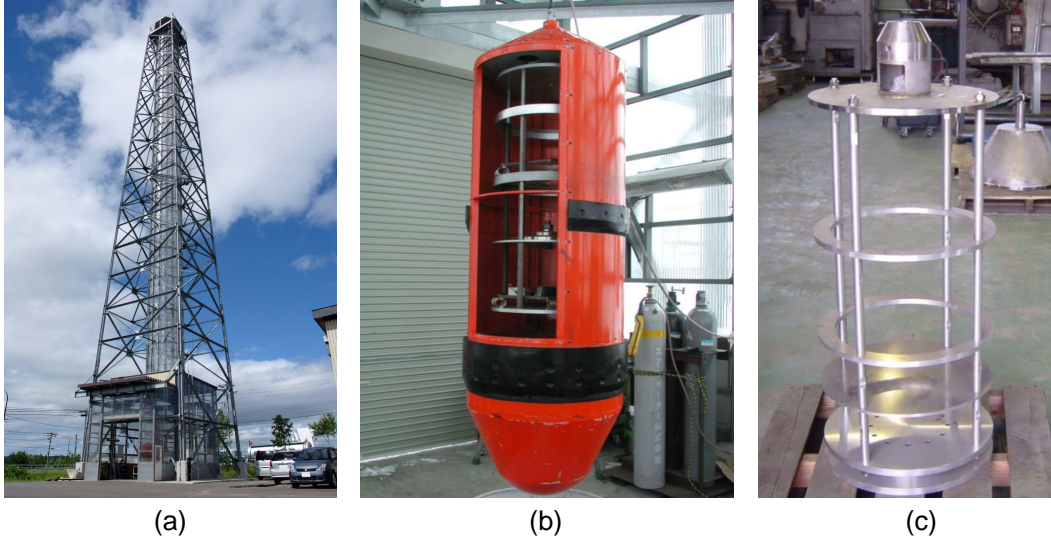


Fig. 1 (a) COSMOTORRE, (b) an outer capsule, (c) an inner capsule

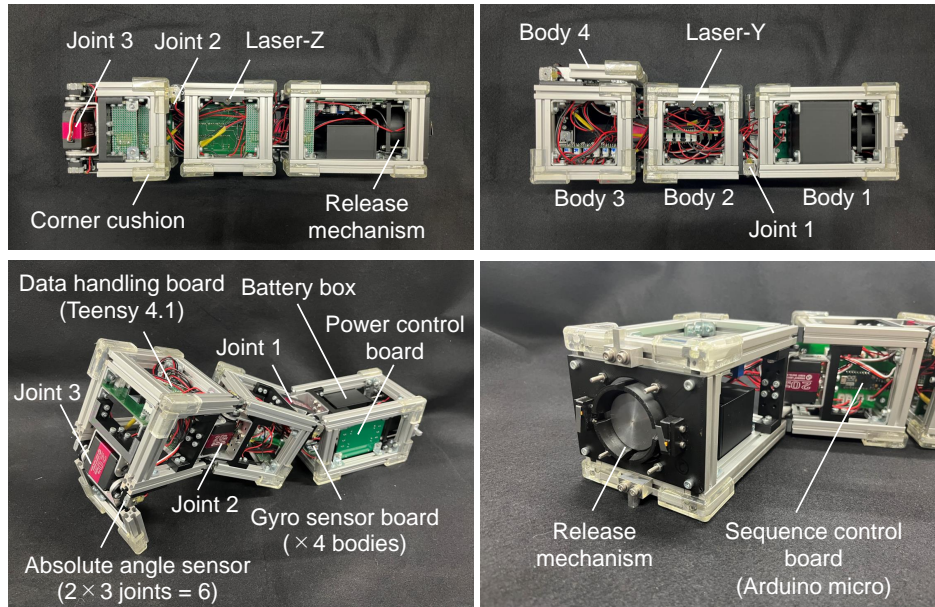


Fig. 2 Overview of the transformable robot

data handling board, specializes in data acquisition from MEMS gyroscopes and absolute angle sensors and data recording on an SD card. This separation of the roles enables the robot to achieve

a sampling rate of about 280 Hz, which is sufficiently fast in this experiment.

2.3 Design of the release mechanism

The release mechanism is designed to satisfy the following requirements:

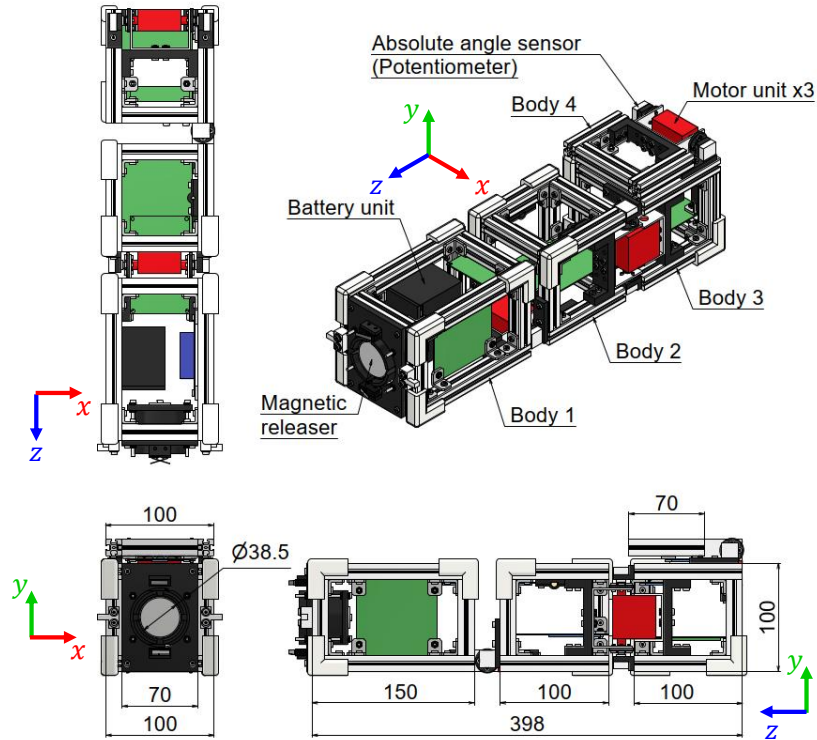


Fig. 3 Dimensions of the transformable robot

1. To stably hold the robot until the beginning of the microgravity experiment
2. To provide detaching force to overcome residual magnetic force under micro-gravity
3. To push the robot with the proper vertical velocity at releasing
4. To suppress transversal releasing velocity to prevent the robot from touching the frame structure during the entire maneuver

Figure 4 shows the overview of the designed release mechanism.

The robot is attached to the electromagnet unit with the magnetic plate of SUS440C. The

electromagnet, Kanetec KE-3HA, provides a magnetic force of 200 N (20.4 kgf) at a maximum, which can sufficiently hold the robot weighing about 3 kg. However, an extra holding mechanism with nylon wires shown in Fig. 5 is attached because higher acceleration is added when a crane lifts the capsule. After crane lifting is completed, the nylon wire is tied firmly between hooks and burned by a nichrome electric heating wire. Tensile force on the nylon wires is applied by sliding the position of wire tensioners, which enables tight holding and secure cutting. Requirement 1, shown above, is satisfied with this electromagnet and nylon wire holding mechanism.

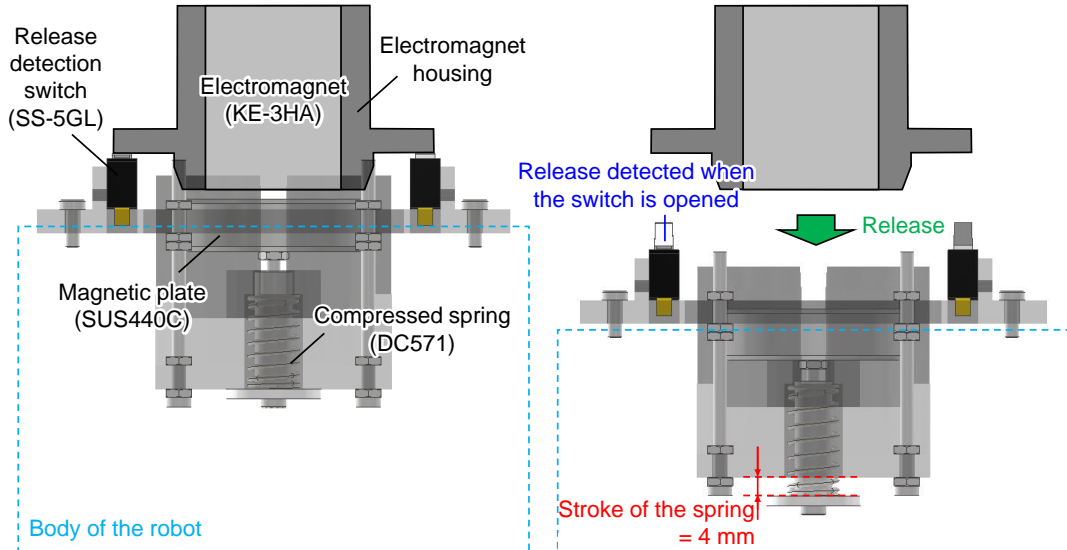


Fig. 4 Overview of the magnetic releaser

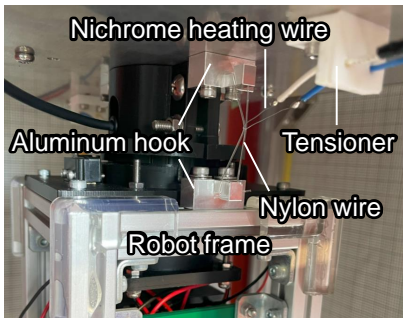


Fig. 5 Holding mechanism with nylon wire

The magnetic plate is connected to the shaft with a spring and fits in the 3D-printed housing structure. The spring is compressed when the robot is attached, and thus, it provides detaching force to overcome residual magnetic force under micro-gravity. The residual magnetic force is estimated as 5% of the maximum magnetic force, hence 10 N, according to the datasheet. The designed spring mechanism provides 11.1 N, which can give sufficient detaching force under micro-gravity. In addition, the stroke of the spring is

set to 4 mm, which can give sufficient separation distance (1 mm is enough according to the datasheet). Requirement 2 is satisfied with this mechanism.

Two release detection switches (OMRON SS-5GL) are equipped beside the magnetic plate. The switches are closed when the robot is attached to the electromagnet and opened when released. The robot starts a preset sequence after detecting the switching. In addition, the switches slightly push off the robots at the release and provide proper vertical velocity. If the vertical velocity is small, the robot must wait very long until the beginning of movement to prevent itself from colliding with the magnetic releaser. On the other hand, if the vertical velocity is too large, the robot collides with the bottom of the test space before the end

of the attitude maneuver. Thus, the proper vertical velocity range is estimated as $20 < v_0 < 100$ mm/s.

Figure 6 illustrates the relationship between pushing force and stroke of a switch lever. Moreover, the figure shows relationships of some operational characteristics: OF (operation force), RF (releasing force), PT (pre-travel), OT (over-travel), MD (movement differential), FP (free position), OP (operating position), RP (releasing position), and TTP (total travel position).

The properties of SS-5GL are shown in Table 3. From these properties, we can estimate the kinetic energy K provided by the switches by calculating the area enclosed by the thick lines in the graph of Fig. 6. It is estimated as $2.35 < K < 3.12$ mJ with two switches, corresponding to a vertical releasing velocity of $40.6 < v_0 < 46.8$ mm/s. The actual vertical velocity observed in the test was distributed in the $30 < v_0 < 50$ mm/s because other factors, such as contact friction force between electromagnet housings, are complicated. However, the range is always within the required level, and thus, we concluded that requirement 3 is satisfied with this design.

Figure 7 shows the relationship between the maximum maneuver envelope and permissible displacement during the maneuver. The release mechanism is required to release the robot as the transversal velocity is under the permissible level to prevent the robot from colliding with walls and

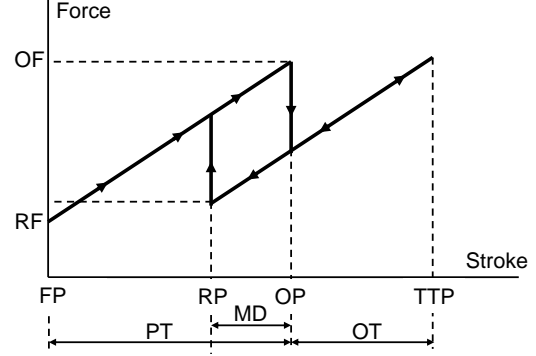


Fig. 6 Force-stroke plot for release detection switches

Table 3 Operating properties of OMRON SS-5GL

OF max.	0.49 N
RF min.	0.06 N
OT min.	1.2 mm
MD max.	0.8 mm
FP max.	13.6 mm
OP	8.8 ± 0.8 mm

pillars. In this experiment, the radius of the minimum envelope is 165 mm, whereas the maximum envelope of the robot during an entire maneuver is 100 mm. Thus the permissible transversal releasing velocity v_p during is calculated as:

$$\begin{aligned}
 v_p &= \frac{r_f - d_m}{t_{\text{maneuver}}} \\
 &= \frac{165\text{mm} - 100\text{mm}}{2.5\text{s}} = 26\text{mm/s}
 \end{aligned} \tag{1}$$

Throughout the preparation test, we confirmed that the designed releasing mechanism has satisfied this requirement. In the actual test shown in Section 5, the transversal velocity was about 7 mm/s, and it is confirmed that there were no collisions with walls and pillars.

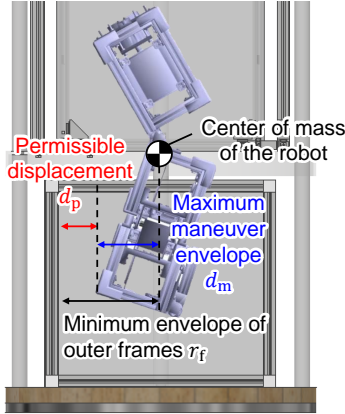


Fig. 7 Permissible transversal displacement of release

3 Maneuver design

This section describes the design of the reorientation maneuver adopted in the experiment. First, we overview the principles of attitude reorientation and a fundamental maneuver in Section 3.1. Section 3.2 denotes the physical modeling of the robot.

3.1 Nonholonomic attitude reorientation

The dynamics of free-floating multibody have been intensively investigated. It is known that the free-flying multibody can reorient itself by a proper sequence of joint actuation, even if the total angular momentum has always been kept at zero. Historically, it is known by righting reflex of falling cats (Muller and Weed, 1916; McDonald, 1955; Kane and Scher, 1969), and intensively studied for space robots with robotic manipulators (Murray and Sastry, 1993; Dubowsky

and Papadopoulos, 1993; Nakamura and Mukherjee, 1993; Papadopoulos, 1993; Mukherjee and Kamon, 1999). The angular momentum conservation law imposed on the free-flying robot is nonholonomic, which means the robot’s final attitude depends on the procedure of joint actuation. Therefore, the robot can arbitrarily reorient its attitude by designing proper joint actuation maneuvers.

In this experiment, we adopt a maneuver similar to the one proposed in previous research, such as Ohashi et al (Aug. 2018); Kubo and Kawaguchi (2022). Two examples of joint actuation are shown in Fig. 8. The sequence shown in the upper side is composed of four consecutive joint actuations, where the first stroke and third strokes are actuations of the same joint but in the opposite direction ($\Delta\theta_1 = +\alpha$ and $-\alpha$), and so do the second and fourth strokes ($\Delta\theta_2 = +\beta$ and $-\beta$). The attitude is reoriented due to the nonholonomy of the system, and thus it is referred to as *nonholonomic attitude reorientation*. The one in the lower is composed of four consecutive joint actuation, but the first and fourth strokes are the same pattern as the second and third strokes. This sequence exactly cancels the intermediate attitude difference, and therefore, attitude is not reoriented after the four strokes. These two examples show that the final attitude depends on the intermediate joint actuation sequence.

The corresponding trajectory in a joint angle space is shown in the left side of Fig. 8. A joint angle space is a multi-dimensional space where each point corresponds to one set of joint states. In these examples, the maneuvers are expressed as a consecutive rectilinear path. If the path draws a closed polygon as in the upper case in Fig. 8, the joint state of a robot returns to the initial state, whereas attitude is changed from the initial. This closed-loop actuation is adopted in this experiment because it clearly shows the effect of reorientation due to the nonholonomy of the system.

3.2 Physical modeling of the robot

This section describes how to model physical properties such as center of mass, moment of inertia, and joint positions of joints. These properties are necessary to design optimal reorientation maneuvers in Section 3.3.

We modeled the robot based on the following assumptions:

- Actual measurement value by an electric scale is used for a mass of each component
- Center of mass and moment of inertia of each component are calculated assuming the component has homogeneous density
- Movable components such as wires are not included in the model

Figure 9 shows the definitions of global body frames and local body frames, indicating the origins and orientations of the frames. The origins are attached to the corner point of the aluminum frame. Table 4 shows the positions of the rotational axes of joints in the global frame. Note that the axes are aligned parallel to x or y in the global frame. Therefore, for example, the x position of joint 1 is not indicated since the axis is parallel to the global x axis. Table 5 shows the positions of the center of mass of each body in the local body frame. Table 6 is the moment of inertia of each body around the local center of mass in the local body frame.

Table 4 Positions of rotational axes of joints in the global body frame (unit: mm)

	x	y	z
Joint 1	-	9.9	236.0
Joint 2	90.1	-	112.0
Joint 3	-	112.0	10.0

Table 5 Positions of the center of mass of each body in the local body frame (unit: mm)

	x	y	z
Body 1	46.58	50.93	84.18
Body 2	47.86	46.68	54.36
Body 3	52.76	53.17	48.77
Body 4	50.50	6.59	31.00

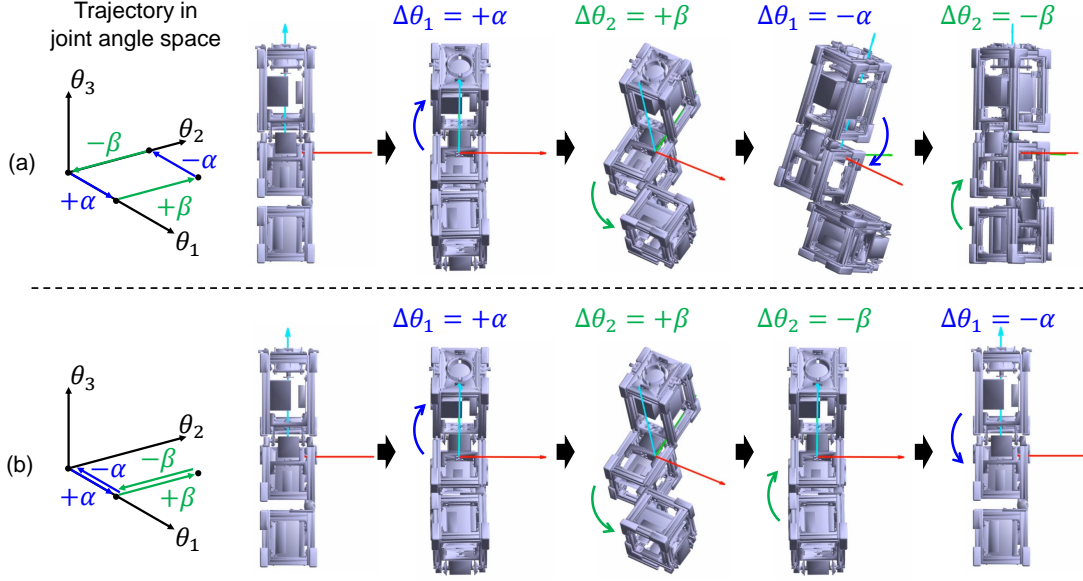


Fig. 8 Two examples of joint actuation (a): with reorientation, (b): without reorientation

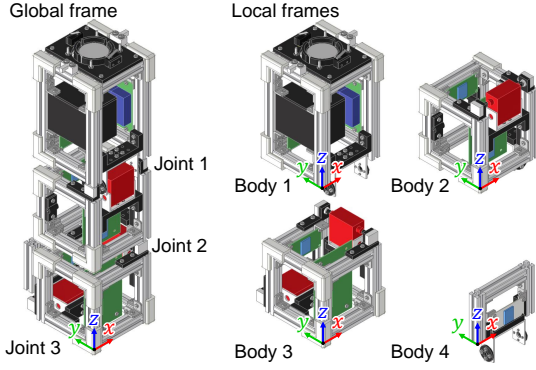


Fig. 9 Definitions of global body frame and local body frames

Table 6 Moment of inertia of each body around the local center of mass in the local body frame (unit: $\text{g} \cdot \text{m}^2$)

	I_{xx}	I_{xy}	I_{xz}	I_{yy}	I_{yz}	I_{zz}
Body 1	3.97	-0.01	-0.08	4.10	0.09	2.27
Body 2	1.72	0.00	-0.07	1.67	0.08	1.56
Body 3	2.00	-0.01	-0.09	1.94	0.09	1.80
Body 4	0.12	0.00	0.00	0.28	-0.01	0.17

3.3 Design of optimal reorientation maneuver

We derive optimal reorientation maneuvers based on the model described in Section 3.2. The optimization is essential due to the following reasons:

- The robot must complete the entire reorientation sequence within a very short duration of micro-gravity (around 2.5 seconds)
- It is necessary to achieve as large joint angle displacement as possible to observe the nonholonomic reorientation effect clearly

In this experiment, we adopted the particle swarm optimization (PSO). PSO is a bio-inspired heuristic optimization method proposed in [Kennedy and Eberhart \(1995\)](#). The formulation is simple and requires no gradient information for the objective function. Moreover, it is easily extensible to

the robot with more actuatable joints and, thus, directly applicable in future missions.

The joint actuation sequence is expressed as a closed loop in a joint angle space as described in Section 3.1. A schematic of an example of joint actuation sequence is shown in Fig. 10. A point in the joint angle space corresponds to a set of specific joint angles. Angles of joints 1, 2, and 3 are denoted as $\theta_1, \theta_2, \theta_3$ whereas input joint angle displacements are denoted as $\alpha_1, \alpha_2, \alpha_3 > 0$ respectively. Specifically, Fig. 10 shows the case of $(i, j, k) = (3, 2, 1)$, $+\alpha_i \rightarrow +\alpha_j \rightarrow +\alpha_k \rightarrow -\alpha_j \rightarrow -\alpha_i \rightarrow -\alpha_k$. For a certain set of $(\alpha_1, \alpha_2, \alpha_3)$, the total number of combinations of joint actuation sequence is 30, as shown in Fig. 11. Note that $-\alpha_i$ is not chosen just after $+\alpha_i$ because it does not induce any attitude difference.

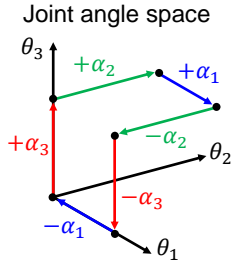


Fig. 10 An example of joint actuation sequence (the case of $(i, j, k) = (3, 2, 1)$, $+\alpha_i \rightarrow +\alpha_j \rightarrow +\alpha_k \rightarrow -\alpha_j \rightarrow -\alpha_i \rightarrow -\alpha_k$)

The optimization problem is defined as Eq. (2). The objective function J is evaluated by the magnitude of attitude difference $\Delta\phi$ and the penalty on maneuver time overrun $P(\max[T - T_{\max}, 0])^2$. If P is large, the maneuver time overrun is avoided

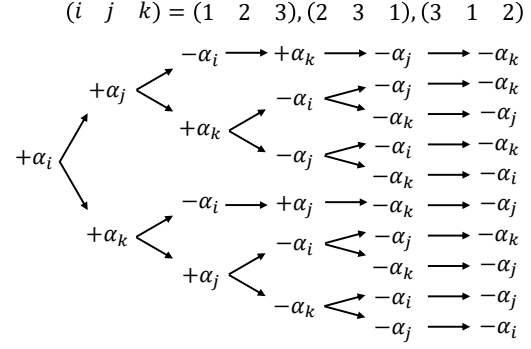


Fig. 11 All sequence pattern for a certain set of (i, j, k)

more strictly. In this experiment, $P = 10^{11}$ is chosen as a sufficiently large value. T_{\max} is set to 1.5 sec, assuming a 1.0 sec margin should be included in the total 2.5 sec duration.

$$\begin{aligned} \underset{\alpha_1, \alpha_2, \alpha_3}{\text{minimize}} \quad & J = \min_C \left(-\Delta\phi + P(\max[T - T_{\max}, 0])^2 \right) \\ \text{subject to} \quad & 0 \leq \theta_{1,2,3} \leq 90 \text{ deg}, \\ & (\theta_1, \theta_2, \theta_3) = (0, 0, 0) \text{ deg at } t = 0 \end{aligned} \quad (2)$$

Applying PSO to the free-floating robot defined in Section 3.2, we obtained the optimized maneuver as shown in Fig. 12. Optimized joint angle displacements are $(\alpha_1, \alpha_2, \alpha_3) = (58.75, 70.29, 0.00)$ degrees. The average angular velocity of the joint is set to be 170 deg/s, resulting in 1.50 sec of the entire maneuver time. The resulting maneuver is composed only of 4 strokes because α_3 is degenerated into 0 degrees through the optimization. This is because the moment of inertia of body 4 is smaller than others by one order as in Table 6, and thus, the actuation of joint 3 is omitted in the

limited maneuver time. The total attitude difference is 26.11 degrees in the z axis. The resulting maneuver is tested in the drop tower test as shown in Section 5. In the actual test, the values of the joint angle displacements commanded to motors are rounded as $(\alpha_1, \alpha_2) = (59, 70)$ to simplify the operations of the microprocessor.

3.4 Design of experiment sequence

Finally, we construct an entire sequence of the experiment with the resulting maneuver in Section 3.3. Table 7 shows the designed experiment sequence.

First, the capsule is dropped by the ground command. At almost the same time, the robot is released by the electromagnet controller that detects the microgravity. Soon, the release detection switch is opened, and the robot starts the movement sequence. These events occur almost simultaneously; thus, we ignore the delay between these events. The robot pauses to prevent touching the release mechanism during the first joint actuation. As described in Section 2.3, the worst (slowest) vertical releasing velocity is estimated as about 30 mm/s. Thus, the pausing time is set to be 0.7 seconds to guarantee the robot does not collide with the releaser, even in the worst case.

After the pausing, the robot starts the maneuver designed in Section 3.3. The interval between the actuation is calculated as the joints move at 170 deg/s on average. After the four strokes, the

robot pauses the joint actuation and continues MEMS gyroscope and joint angle data recording until the deceleration of the capsule.

4 Setups for the experiment

4.1 Arrangement in the inner capsule

Figure 13 shows the arrangement in the inner capsule. All the equipments are mounted within the envelope of the inner capsule. The test area is about 830 mm in height and 500 mm in diameter, providing sufficient space for the robot to move without touching any structures. Two action cameras (GoPro HERO9) are mounted vertically and capture the robot's motion during the sequence. Two graph papers are attached to the side walls that work as the projection screen of lasers mounted on the body 2. The trajectories of the laser lays are captured by two additional action cameras that are used to estimate the vertical releasing velocity of the robot. A cushion is placed at the bottom of the test space, which reduces damage to the robot at landing. Other electric components to control the experiment sequence are placed on the wooden platform deck above the test space.

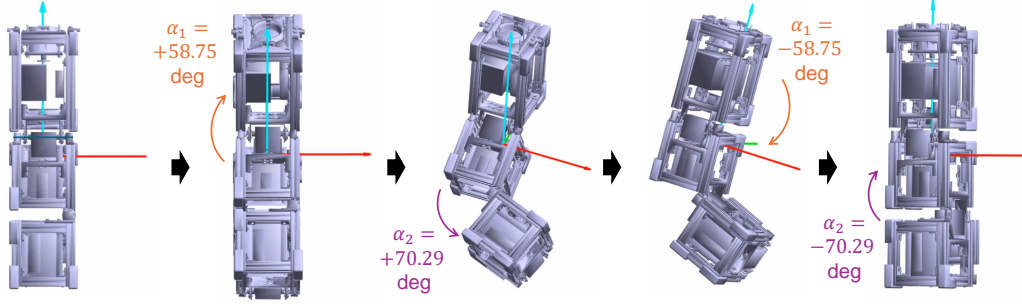


Fig. 12 The maneuver generated by the PSO

Table 7 Designed experiment sequence

Sequence	Time [sec]	Events
0	0.00	Capsule dropped, electromagnet released, and release detected
1	0.70	Joint 1 commanded to be actuated (+59 degrees)
2	1.05	Joint 2 commanded to be actuated (+70 degrees)
3	1.47	Joint 1 commanded to be actuated (-59 degrees)
4	1.82	Joint 2 commanded to be actuated (-70 degrees)
5	2.23	Maneuver finished, and data recording maintained
6	2.50	Drop capsule decelerated at landing

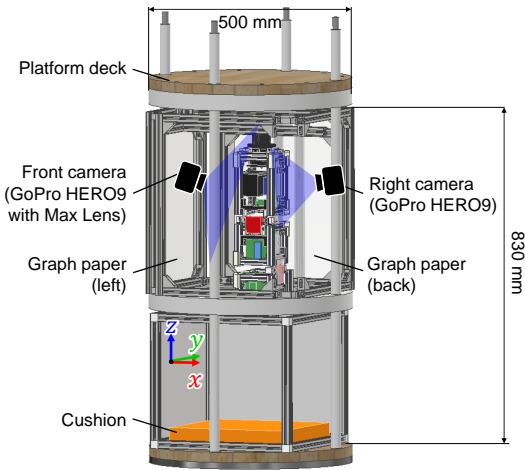


Fig. 13 Configuration of the inner capsule

4.2 Calibrations

All absolute angle sensors and MEMS gyroscopes are calibrated before each test trial because every landing impact can affect their measurements.

The absolute angle sensors are mainly used to provide a zero-point of the joint angles. The zero-point value is measured by applying an attachment that holds the frames between bodies (Fig. 14).

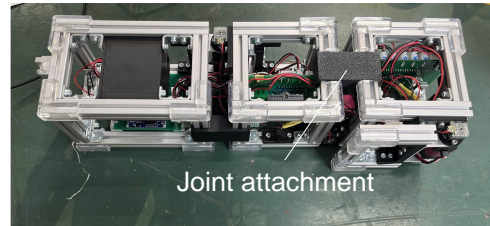


Fig. 14 Joint holding attachment for joint angle calibration

Calibration of the MEMS gyroscope is essential to guarantee the accuracy of measurement. In general, the primary error factors of MEMS gyroscopes are zero-rate output bias, scale factor

tolerance, misalignment of axes, and acceleration sensitivity. First, zero-rate output bias can be measured and trimmed a few minutes before the drop of the capsule. The duration of the test (2.5 sec) and the waiting time until a drop (a few minutes) are both sufficiently short. Therefore, the bias error is expected to have a relatively small influence compared to other factors.

The scale factor is not calibrated in this experiment, and thus, $\pm 3\%$ error is included in the data as shown in Table 2. In addition, the influence of linear acceleration sensitivity is neither compensated because the gyroscope measurement is performed in microgravity and is not dependent on attitude with respect to the gravity direction.

Misalignment error is removed by measuring cross-axis correlations. Figure 15 shows an example of the cross-axis correlation measurement. In this case, body 1 is rotated along joint 1, whereas bodies 2, 3, and 4 are fixed on the ground. If the MEMS gyroscope on body 1 is ideally aligned to the rotational axis of joint 1, it exhibits the angular velocity of the x component. However, the actual measurement shows correlations of y and z components due to misalignment. By measuring the cross-axis correlations for two orthogonal axes on each body, the actual mounted attitude of the MEMS gyroscope can be estimated. All movement patterns for the misalignment calibration

are shown in Table 8. These patterns cover measurements for two orthogonal axes on each body.

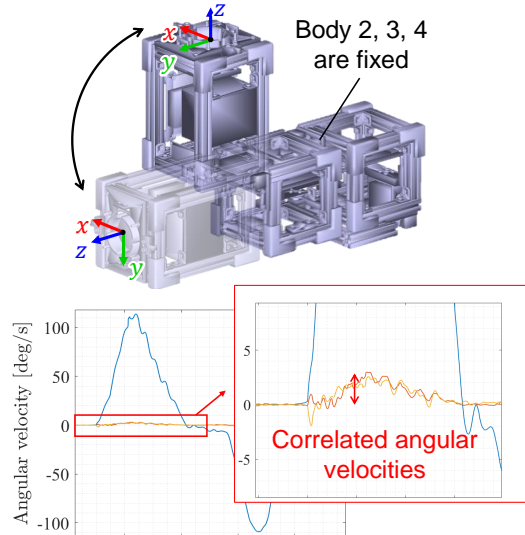


Fig. 15 Example of cross-axis correlation measurement (body 1 is rotated along joint 1)

Table 8 Motion patterns for misalignment calibration

Rotational axis	Moved bodies
Joint 1	Body 1
Joint 1	Body 2, 3
Joint 2	Body 1, 2
Joint 2	Body 3, 4
Joint 3	Body 4

5 Result

This section describes the results of the drop tower test and evaluates the numerical model with the obtained data.

Figure 16 shows sequentially captured images by the front and the right cameras. The time

stamps of the images are based on the sequence shown in Table 7. The figure shows that the robot’s attitude is reoriented after four strokes of joint actuation as described in Section 3.1. In addition, we confirmed by the video that the robot did not collide with any structures during an entire maneuver.

Data of MEMS gyroscopes was successfully sampled in about $f_s = 280$ Hz on average. The obtained angular velocities from all bodies are processed as shown in Fig. 17. The upper left figure is z - y - x Euler angles of body 1, calculated by integrating the angular velocity of body 1 shown in the upper right. Initial angular velocity $\boldsymbol{\omega}_0$ after the release was about $[\omega_{x0}, \omega_{y0}, \omega_{z0}] = [-0.73, -0.48, -0.77]$ deg/s. Total attitude reorientation after four joint strokes was 23.3 degrees, whereas the ideal reorientation angle of the designed maneuver is 26.1 degrees as described in Section 3.3. This gap is generated by the initial angular velocity and the difference between the commanded joint displacements and the actual (described below).

The lower left figure is a history plot of joint angles. Initial angles are sampled from the absolute angle sensors, and displacements from them are calculated by integrating relative angular velocities derived by subtracting outputs of adjacent gyroscopes. Note that the initial angle of joint 1 has an offset of about +6 degrees due to gravity torque applied before a drop. In addition, joint

displacements do not precisely follow the angles shown in Table 7; e.g., the actual displacement of the first stroke is 54.8 degrees, whereas the commanded angle is 59.0 degrees. This is because the reproducibility performance of our servomotor was not high. However, the obtained result is still valid because we can evaluate the numerical model by performing numerical integration with the actual joint angle displacements.

The lower right figure shows the total angular momentum of all bodies in the inertial frame, which is calculated with the obtained data and the numerical model described in Section 3.2. Ideally, the angular momentum should be conserved throughout the entire sequence, and the values before $t = 0.7$ and after $t = 2.5$ have agreed well. During $0.7 < t < 2.5$, the conservation quality gets worse due to the influence of joint actuation. The influence of linear acceleration and vibration on MEMS gyroscopes seems to induce high-frequency noise. In contrast, low-frequency noise seems to be caused by modeling errors, such as the position of the center of mass of each body.

The latter error can be suppressed by compensating the modeling error of the center of mass of each body. Thus, we solved an optimization problem defined in Eq. (3) to obtain a proper offset of the center of mass. Optimized variables are $\delta \mathbf{r}_{Gi} = [\delta x_{Gi}, \delta y_{Gi}, \delta z_{Gi}]$, position offsets of center of mass in the local frame of i -th body ($i =$

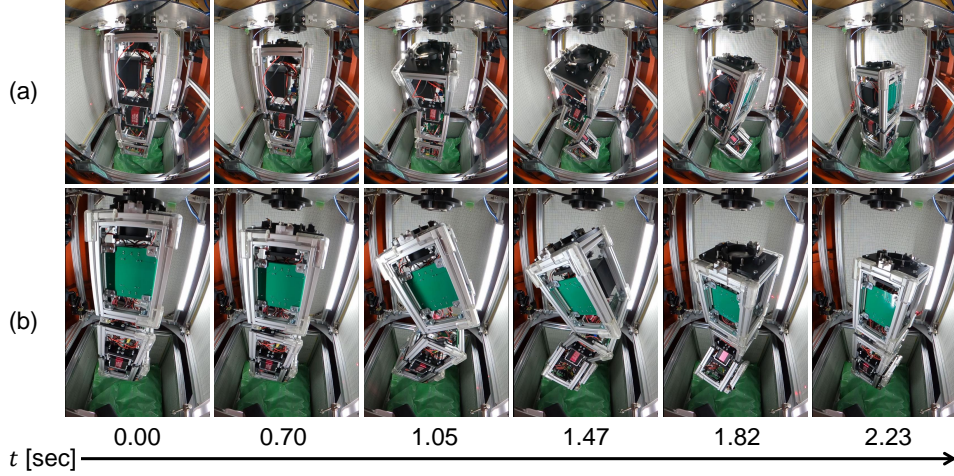


Fig. 16 Sequentially captured images (a): front camera, (b): right camera

1, 2, 3, 4). $\bar{\mathbf{h}}_{t_j}$ denotes total angular momentum of the robot at $t = t_j$ and the bar $\bar{\cdot}$ signifies moving average of local N -points. Thus, the objective function is the sum of the norm of the difference between moving-averaged angular momentum at $t = t_j$ and $t = t_0$ for all sampling points. The moving average works as a simple low-pass filter and its width of averaging window N is determined as it satisfies the appropriate cutoff frequency. In this case, $N = 25$ is set; it corresponds to cutoff frequency $f_{co} = 5$ Hz in sampling frequency $f_s = 280$ Hz (Smith, 1999). $d_{xi}, d_{yi}, d_{zi} > 0$ are magnitudes of maximum offsets. We set $d_{xi}, d_{yi}, d_{zi} = 10$ mm for $i = 1, 2, 3$ and $d_{x4}, d_{y4}, d_{z4} = 0$ mm because the body 4 does not move with respect to the body 3 in this maneuver. Table 9 shows the optimization

result.

$$\begin{aligned}
 & \underset{\delta \mathbf{r}_{G_i} (i = 1-4)}{\text{minimize}} && J = \sum_j |\bar{\mathbf{h}}_{t_j} - \bar{\mathbf{h}}_{t_0}| \\
 & \text{subject to} && -d_{xi} \leq \delta x_{Gi} \leq d_{xi}, \\
 & && -d_{yi} \leq \delta y_{Gi} \leq d_{yi}, \\
 & && -d_{zi} \leq \delta z_{Gi} \leq d_{zi}, \\
 & && (i = 1-4)
 \end{aligned} \tag{3}$$

Figure 18 shows a comparison of angular momen-

Table 9 Optimal offset of the center of mass in local frames (unit: mm)

Body number	x	y	z
Body 1	-2.24	0.92	2.99
Body 2	-2.37	-0.12	7.10
Body 3	-2.76	-1.05	4.92
Body 4	0.00	0.00	0.00

tum between before and after the modeling error compensation; the upper figures are time-domain, and the lower are frequency-domain spectrum transformed by fast Fourier transformation, FFT

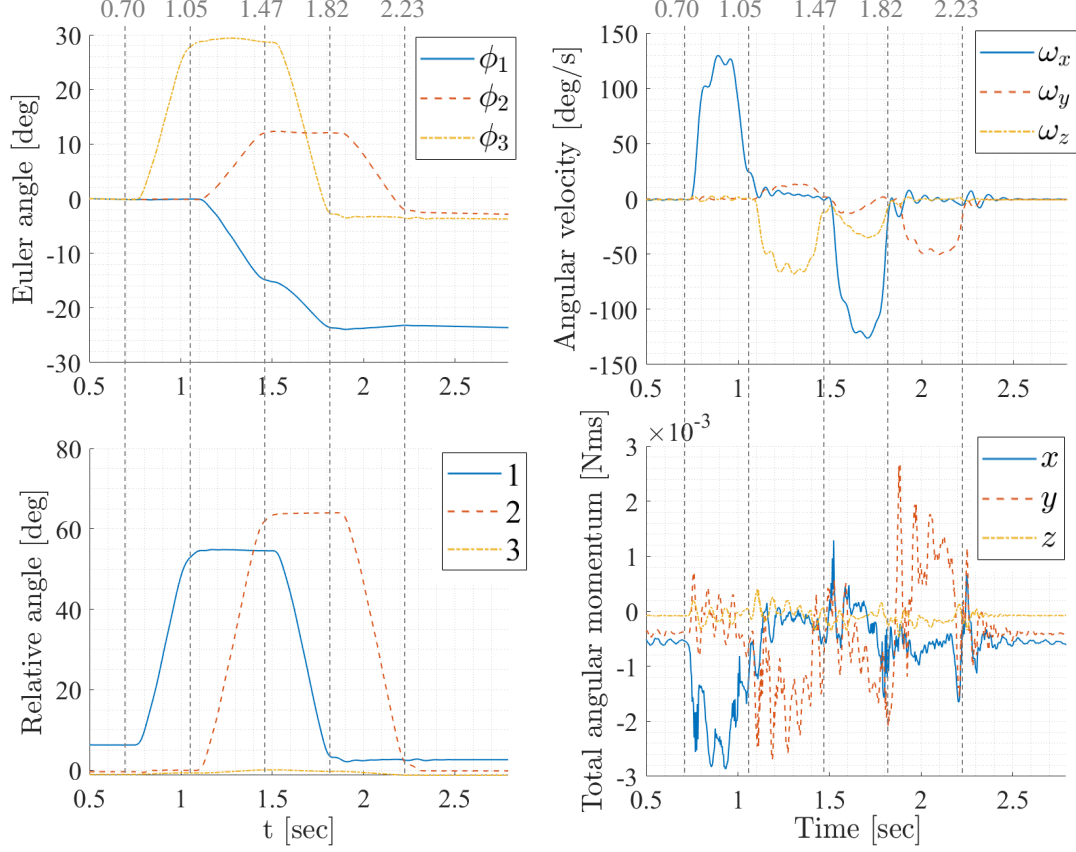


Fig. 17 Upper left: attitude of body 1 (z - y - x Euler angles), upper right: angular velocity of body 1, lower left: joint angles, lower right: total angular momentum

(Frigo and Johnson, 1998). The enclosed areas in the lower figure show that the compensation successfully suppressed the low-frequency noise below $f_{co} = 5$ Hz.

Finally, we move on to evaluating the robot’s numerical model. We can derive the equation of motion for the attitude of body 1 with angular momentum conservation and modeled physical properties shown in Section 3.2. The equation of motion is integrated with the initial attitude of body 1 and the history of joint angles. By comparing the solution of the equation of motion and

the attitude directly integrated from the angular velocity of the body 1 (shown in Fig. 17), we can evaluate the accuracy of the numerical model defined in Section 3.2.

Figure 19 compares the frequency spectrum of angular velocity error between before and after modeling error compensation. As with angular momentum, the compensation successfully suppresses low frequency error below $f_{co} = 5$ Hz. Figure 20 compares z - y - x Euler angles’ error between before and after modeling error compensation. The compensation suppressed the attitude difference in the entire maneuver. Thus,

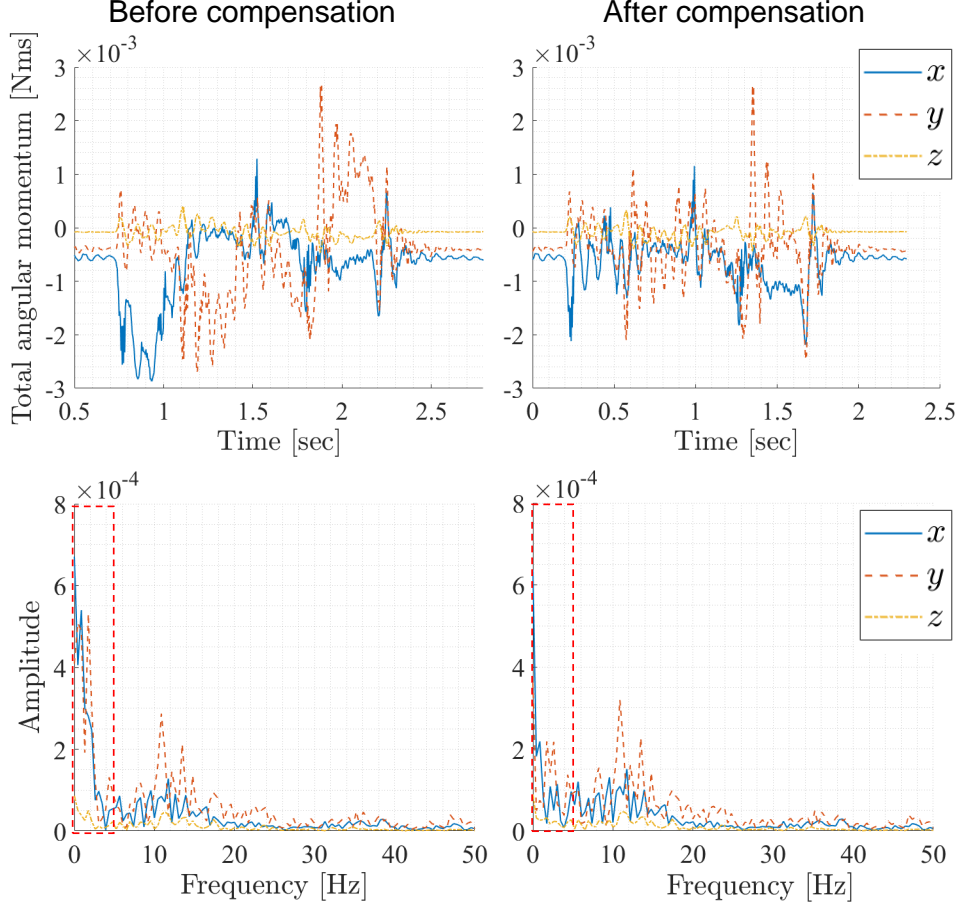


Fig. 18 Comparison of angular momentum between before and after modeling error compensation (upper: time history, lower: frequency spectrum, left: before compensation, right: after compensation)

we concluded that the designed modeling error compensation has successfully worked.

6 Discussion

Although the hardware we used in this experiment was different from the actual flight hardware, modeling, maneuver design, and calibration methods are commonly applicable to 3U CubeSat orbit demonstrations. This section discusses the difference between the drop tower test and the orbit demonstration.

6.1 Feedback control

In the drop tower test, the robot was supposed to perform a feedforward maneuver because the duration allowed for the maneuver was strictly limited. In the orbit demonstration, however, the robot has sufficient time to perform feedback control to achieve the target attitude. A fundamental feedback control method is a successive table lookup of motion primitives (Ohashi et al, Aug. 2018). In each lookup, the spacecraft estimates the difference between the current and the target

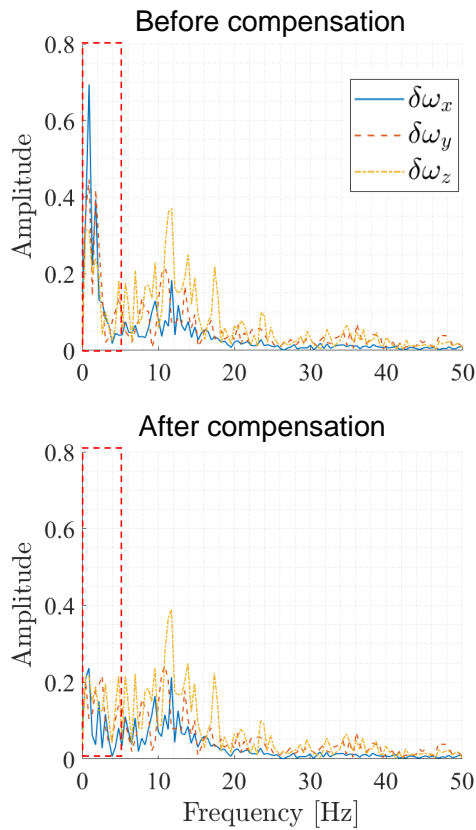


Fig. 19 Comparison of frequency spectrum of angular velocity error between before and after modeling error compensation

attitude and selects the best motion primitive to approach the target. The accuracy of the numerical model determines the accuracy of achieving the target attitude to construct the motion primitive table. Figure 20 in Section 5 shows that the spacecraft is expected to achieve the target attitude at least within 1 degree accuracy.

6.2 Modeling error compensation

In the drop tower test, the availability of modeling error compensation is limited because the

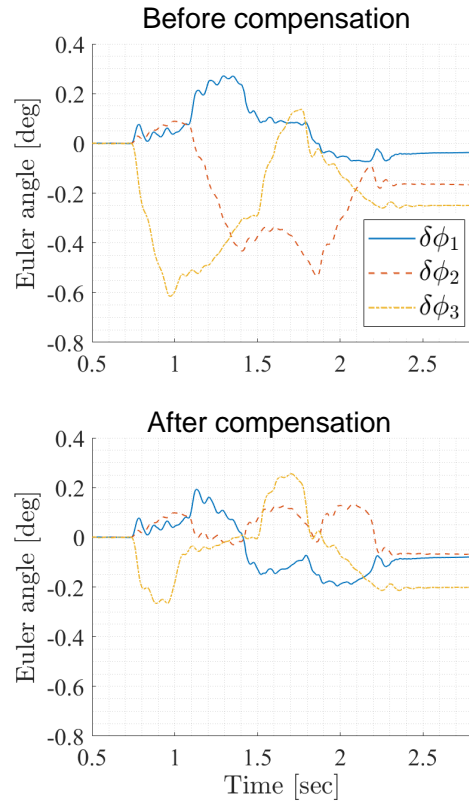


Fig. 20 Comparison of Euler angles' error between before and after modeling error compensation

maneuver time is very short, and the robot configuration is inconsistent through trials due to structural damage experienced at every landing. In the orbit demonstration, however, more accurate compensation is expected to be possible. As well as the center of mass, the moment of inertia can be predicted by analyzing a longer series of data. A more accurate model helps the spacecraft to achieve more accurate reorientation as described in Section 6.1.

6.3 Error of gyroscopes

We chose cost-effective MEMS gyroscopes in this experiment because many spares must be prepared due to strong landing impacts. We can expect to use high-performance MEMS IMU for the orbit demonstration. The comparison of the major specifications between MPU-6050 and ADIS16465-2 (an example of the high-performance IMU) is shown in Table 10. Obviously, ADIS16465-2 performs much better than MPU-6050; in particular, linear acceleration sensitivity is about 10 times better. Thus, we can expect the high-frequency noise seen in Fig. 18 and 19 to be suppressed with such high-performance IMUs.

Table 10 Specification comparison between MPU-6050 and ADIS16465-2 (the value shown in '-' is not specified in datasheet)

Parameters	MPU-6050	ADIS16465-2
Full-scale range	± 500 deg/s	± 500 deg/s
Full-scale bit length	16 bits	32 bits
Bias stability	-	2.5 deg/hour
Linear acc. sensitivity	0.1 deg/s/g	0.009 deg/s/g

7 Conclusion

The purpose of this research was to construct an evaluation method for a numerical model for a transformable spacecraft using a drop tower facility. We introduced the design of the experiment and exhibited the results and analyses. The results showed that our numerical model

replicated the robot's motion within 1 degree of accuracy. In addition, post-experiment model corrections based on the results further improved the accuracy of the numerical solution. The performance of the hardware we used in this experiment was limited due to cost constraints, and further studies with actual flight hardware would provide a better evaluation of the actual orbit demonstration.

Acknowledgements

The authors would like to thank Uematsu Electric Co., Ltd. for technical assistance with the experiments. This study was funded by a Grant for a strategic research group from the Advisory Committee for Space Engineering in Japan.

Statements and Declarations

- **Funding** This study was supported by the Advisory Committee for Space Engineering in Japan as a strategic research group.
- **Competing interests** This study was funded by a Grant for a strategic research group from the Advisory Committee for Space Engineering in Japan. The authors have no competing interests to declare that are relevant to the content of this article.
- **Ethics approval and consent to participate** Not applicable.
- **Consent for publication** Not applicable.

- **Data availability** The authors declare that the data supporting the findings of this study are available within the paper as supplementary files.
- **Materials availability** Not applicable.
- **Code availability** The authors declare that the source files used in the experiment are available within the paper as supplementary files.
- **Author contribution** All authors contributed to the study conception and design. Material preparation, data collection, and analysis were performed by Tsubasa Ando, Hirona Kawahara, Shu Miyata, Naoya Uchiyama and Yuki Kubo. Design of the optimal maneuver was performed by Kazutoshi Ito. The first draft of the manuscript was written by Yuki Kubo and all authors commented on previous versions of the manuscript. All authors read and approved the final manuscript.

References

- Dubowsky S, Papadopoulos E (1993) The kinematics, dynamics, and control of free-flying and free-floating space robotic systems. *IEEE Transactions on robotics and automation* 9(5):531–543
- Frigo M, Johnson SG (1998) Fftw: An adaptive software architecture for the fft. In: *Proceedings of the 1998 IEEE International Conference on Acoustics, Speech and Signal Processing, ICASSP'98* (Cat. No. 98CH36181), IEEE, pp 1381–1384
- Kane T, Scher M (1969) A dynamical explanation of the falling cat phenomenon. *International journal of solids and structures* 5(7):663–670. [https://doi.org/10.1016/0020-7683\(69\)90086-9](https://doi.org/10.1016/0020-7683(69)90086-9)
- Kennedy J, Eberhart R (1995) Particle swarm optimization. In: *Proceedings of ICNN'95-international conference on neural networks*, iee, pp 1942–1948
- Kobayashi D, Watanabe K, Kobayashi H, et al (2024) Lessons learned in the operation of the hibari: Variable shape satellite. In: *Proceedings of Small Satellite Conference*
- Kubo Y, Kawaguchi J (2022) Nonholonomic reorientation of free-flying space robots using parallelogram actuation in joint space. *Journal of Guidance, Control, and Dynamics* 45(7):1–11. <https://doi.org/10.2514/1.G006511>, URL <https://doi.org/10.2514/1.G006511>, <https://doi.org/10.2514/1.G006511>
- McDonald D (1955) How does a falling cat turn over. *American Journal of Physiology* 129:34–35
- Mukherjee R, Kamon M (1999) Almost smooth time-invariant control of planar space multi-body systems. *IEEE Transactions on Robotics*

- and Automation 15(2):268–280. <https://doi.org/10.1109/70.760348>
- Muller HR, Weed LH (1916) Notes on the falling reflex of cats. American Journal of Physiology-Legacy Content 40(3):373–379. <https://doi.org/10.1152/ajplegacy.1916.40.3.373>
- Murray RM, Sastry SS (1993) Nonholonomic motion planning: Steering using sinusoids. IEEE transactions on Automatic Control 38(5):700–716
- Nakamura Y, Mukherjee R (1993) Exploiting nonholonomic redundancy of free-flying space robots. IEEE Transactions on Robotics and Automation 9(4):499–506. <https://doi.org/10.1109/70.246062>
- Ohashi K, Chujo T, Kawaguchi J (Aug. 2018) Optimal motion planning in attitude maneuver using non holonomic turns for a transformable spacecraft. In: Proceedings of AAS/AIAA Astrodynamics Specialist Conference, Snowbird, USA, aAS-18-359
- Papadopoulos EG (1993) Nonholonomic behavior in free-floating space manipulators and its utilization. In: Nonholonomic Motion Planning. Springer, p 423–445, https://doi.org/10.1007/978-1-4615-3176-0_11
- Smith SW (1999) The Scientist and Engineer’s Guide to Digital Signal Processing, 2nd edn., California Technical Publishing, chap 15
- Sugawara Y, Chujo T, Kubo Y, et al (Oct. 2020) Transformable spacecraft: Feasibility study and conceptual design. In: Proceedings of the International Astronautical Congress, Virtual, iAC-20-D1.2.8.x59887
- WATANABE K, KOBAYASHI H, AMAKI Y, et al (2023) Flight model development and ground tests of variable-shape attitude control demonstration microsatellite hibari. Journal of Evolving Space Activities 1:103